

CFD Analyses of Textured Surfaces for Tribological Improvements in Hydraulic Pumps

*Original*

CFD Analyses of Textured Surfaces for Tribological Improvements in Hydraulic Pumps / Casoli, Paolo; Scolari, Fabio; Rundo, Massimo; Lettini, Antonio; Rigosi, Manuel. - In: ENERGIES. - ISSN 1996-1073. - ELETTRONICO. - 13:21(2020), p. 5799. [10.3390/en13215799]

*Availability:*

This version is available at: 11583/2854673 since: 2021-03-24T12:06:23Z

*Publisher:*

MDPI

*Published*

DOI:10.3390/en13215799

*Terms of use:*

This article is made available under terms and conditions as specified in the corresponding bibliographic description in the repository

*Publisher copyright*

(Article begins on next page)

## Article

# CFD Analyses of Textured Surfaces for Tribological Improvements in Hydraulic Pumps

Paolo Casoli <sup>1,\*</sup> , Fabio Scolari <sup>1</sup> , Massimo Rundo <sup>2</sup> , Antonio Lettini <sup>3</sup> and Manuel Rigosi <sup>3</sup><sup>1</sup> Department of Engineering and Architecture, University of Parma, 43124 Parma, Italy; fabio.scolari@unipr.it<sup>2</sup> Department of Energy, Politecnico di Torino, C.so Duca degli Abruzzi 24, 10129 Turin, Italy; massimo.rundo@polito.it<sup>3</sup> Casappa Ltd., Via Balestrieri 1, Lemignano di Collecchio, 43044 Parma, Italy; lettinia@casappa.com (A.L.); rigosim@casappa.com (M.R.)

\* Correspondence: paolo.casoli@unipr.it

Received: 7 October 2020; Accepted: 4 November 2020; Published: 5 November 2020



**Abstract:** In any hydraulic machine there are lubricated couplings that could become critical beyond certain operating conditions. This paper presents the simulation results concerning textured surfaces with the aim of improving the performance of lubricated couplings in relative motion. The texturing design requires much care to obtain good improvements, and it is essential to analyze both the geometric features of the dimples and the characteristics of the coupled surfaces, like the sliding velocity and gap height. For this purpose, several CFD simulations have been performed to study the behavior of the fluid bounded in the coupling, considering dimples with different shapes, size, and spatial distribution. The simulations consider the onset of gaseous cavitation to evaluate the influence of this phenomenon on the pressure distribution generated by the textured surface. The analyses have pointed out that it is critical to correctly predict the behavior of the textured surface in the presence of local cavitation, in fact, when cavitation occurs, the characteristic time of the transient in which the phase of the fluid change is very rapid and it is comparable to the time taken by the fluid to move from one dimple to the next.

**Keywords:** CFD simulation; textured surfaces; dynamic cavitation

## 1. Introduction

In hydraulic machines, metallic surfaces in relative sliding motion are widespread and hydrodynamic effects are useful to support heavy loads, due to operating conditions and to limit surface wear. It is very important to study innovative solutions able to improve the coupling performance with the aim of extending the machines working range, as well as improve the pump efficiency.

In this work, the benefits that a textured surface could offer have been studied. Texturing a surface means to realize a precise and ordered micro-geometry on a surface to increase the tribological properties [1].

A textured surface obtains several improvements. The geometric effect generates a greater hydrodynamic bearing capacity, due to an increase in the average pressure that is established between the moving surfaces. Furthermore, a lower friction coefficient could be obtained, since there is a smaller contact area and a greater average gap, reducing the overall surface wear. Yu et al. [2] have presented a numerical study on the influence of dimples' shape and orientation on the load capacity and the friction coefficient, reaching good results in terms of tribological improvements.

An additional outcome is the “hollow” effect. The dimples could ensure a reserve of oil, which is useful to avoid breakage of the lubricating film.

To fully exploit the potential of a textured surface, an accurate design of the geometry is essential. The design phase is a tough challenge, due to the high number of variables involved that could influence the performance of the coupling. Moreover, the features of the dimple depend on the type of contact between the two facing surfaces, as well as the operating conditions and fluid properties [3].

Some researchers have already studied these solutions applied mainly to parallel thrust bearings. Rahmani et al. [4] have numerically studied the influence of the distribution of the dimples on the load capacity and friction force of a parallel thrust bearing, showing that good improvements could be achieved by optimizing the surface geometry. Etsion et al. [5] also achieve great results with a numerical model and with the experimental validation applied to a parallel bearing. Other researchers have investigated the effect of surface texturing realized on circumferential seals. Both Kligerman et al. [6] and Razzaque et al. [7] have shown that the dimples are able to generate a hydrodynamic force useful to reduce the seal friction and wear.

Most of the studies on the textured surfaces have been performed using a finite difference method for numerically solving the Reynolds lubrication equation [5,7,8].

In this work, the attention has been focused on the evaluation of the influence that the geometrical characteristics of the dimples have on the tribological properties of the coupling. A detailed analysis regarding the geometric dimensions of the dimples, as well as the gap, has been performed. Moreover, the change of the relative sliding speed between the two coupled surfaces and viscosity of the fluid has been considered in this research. To evaluate all these variables, several three-dimensional CFD simulations have been performed, using ANSYS® CFX to numerically solve the Navier-Stokes equations.

As a further step, the simulations have been carried out considering the phenomenon of gaseous cavitation. In hydraulic applications, some operating conditions able to onset local cavitating phenomena could occur, with serious consequences on the operation of the machines [9–13]. The cavitation represents a negative aspect even in the presence of a textured surface, since it modifies the coupling performance, and in some cases, it could lead to unwanted and counterproductive effects. This phenomenon has been considered by implementing a dynamic cavitation model that provides different times for the release of dissolved air and its subsequent reabsorption. An accurate multiphase fluid model is essential to correctly predict the behavior of the textured surface in the presence of cavitation, since the characteristic times of the cavitation phenomenon are close to the working fluid pressure evolution. In the scientific literature, there are some works that report values relating to the characteristic phase transition times of the fluid. Zwart et al. [14] suggested some values obtained from numerical simulations on several devices and applications. Escaler et al. [15] performed a sensitivity analysis of the Zwart parameters, finding good agreements between simulation results and experimental tests. Del Campo et al. [16] proposed other values from an in deep study of cavitation in external gear pumps; Zhou et al. [17,18] have found other values focusing on the operation of an orifice in a hydraulic circuit, obtaining good agreement with the experimental data [19,20].

This work is structured as follows: At the beginning, there is the analysis of a configuration characterized by a single dimple to understand which geometry is better from the point of view of the bearing capacity. Then the case of full texturing on the entire available surface is analyzed. Finally, the effectiveness of texturing only on a portion of the entire domain is evaluated. The final outlook of this research is to implement textured surfaces on some components inside hydraulic pumps. Lubricated coupled surfaces are present both in external gear pumps and in axial piston pumps, and their working range could be extended exploiting the benefits offered by engineered surfaces.

## 2. Fluid Model

In the CFD analyses performed, the gaseous cavitation phenomenon has been considered, using the Rayleigh-Plesset model. The definition of both the physical and the thermodynamic properties of the fluid is important to correctly model this phenomenon. The fluid adopted is an ISO VG-46 hydraulic oil with the following characteristics, Table 1.

**Table 1.** Fluid properties.

Parameter	Value
Density	850 kg/m <sup>3</sup>
Viscosity (40 °C)	46 mm <sup>2</sup> /s
Specific heat capacity	1950 J/(kg K)

The fluid temperature is assumed to be equal to 40 °C, since the oil viscosity value is defined at this temperature. The flow is modeled as a mixture of air and oil, and the model solves the continuity and momentum equation for the mixture, in addition to the continuity equation for a fraction of air.

Flow is modeled as laminar, due to the high viscosity of the fluid and the very low gap height values. The simulations were considered converged when the residuals of each equation are less than 10<sup>−5</sup>. The entire domain consists of a stationary structured mesh, formed by hexahedral elements, the number of which was established following a sensitivity analysis of the mesh. The main features of all the meshes realized are the following, Table 2:

**Table 2.** Mesh parameters.

Min Element Size	Max Element Size	Average Element Quality	Average Aspect Ratio	Average Orthogonal Quality	Average Skewness
9.00 × 10 <sup>−7</sup>	9.00 × 10 <sup>−6</sup>	3.80 × 10 <sup>−1</sup>	4.73	9.70 × 10 <sup>−1</sup>	7.30 × 10 <sup>−2</sup>

### Cavitation Model

The release of air and the subsequent reabsorption in a liquid has been studied by Del Campo and Zhou [16,18] using the Rayleigh-Plesset model. The Rayleigh-Plesset equation controls the dynamics of a spherical bubble immersed in a liquid. The growth of a gas bubble in a liquid is given by:

$$R_B \frac{d^2 R_B}{dt^2} + \frac{3}{2} \left( \frac{dR_B}{dt} \right)^2 + \frac{2\sigma}{\rho_f R_B} = \frac{p_v - p}{\rho_f} \quad (1)$$

where  $R_B$  represents the bubble radius,  $p_v$  is the pressure in the bubble (assumed to be the air pressure at the liquid temperature),  $p$  is the pressure in the liquid surrounding the bubble,  $\rho_f$  is the liquid density, and  $\sigma$  is the surface tension coefficient between the liquid and air.

The rate of variation of bubble volume could be expressed as follows:

$$\frac{dV_B}{dt} = \frac{d}{dt} \left( \frac{4}{3} \pi R_B^3 \right) = 4\pi R_B^2 \sqrt{\frac{2}{3} \frac{p_v - p}{\rho_f}} \quad (2)$$

While the rate of change of bubble mass is given by multiplying Equation (2) for the air density. Assuming that  $N_B$  are the bubbles present per unit volume, the volume fraction  $r_g$  could be expressed as follows:

$$r_g = V_B N_B = \frac{4}{3} \pi R_B^3 N_B \quad (3)$$

And the interphase mass transfer rate expressed per unit volume is:

$$\dot{m}_{fg} = F \frac{3r_g \rho_g}{R_B} \sqrt{\frac{2}{3} \frac{|p_v - p|}{\rho_f}} \text{sign}(p_v - p) \quad (4)$$

Equation (4) refers to the case of air absorption, while in the case of air release it should be modified. The process is originated at nucleation sites, but when the air volume fraction increases, the nucleation site density should decrease: In the case of aeration,  $r_g$  is replaced by  $R_{nuc}(1-r_g)$ .

$$\dot{m}_{fg} = F \frac{3R_{nuc}(1-r_g)\rho_g}{R_B} \sqrt{\frac{2}{3} \frac{|p_v - p|}{\rho_f}} \text{sign}(p_v - p) \quad (5)$$

where  $R_{nuc}$  is the volume fraction of the nucleation sites. In Equations (4) and (5),  $F$  is an empirical coefficient that determines the intensity of the process and could be different in the case of air absorption,  $F_a$ , or air release,  $F_r$ : In general, absorption is a process that occurs more slowly than release and this aspect is quantified with the  $F$  parameter.

In the scientific literature, the values of the parameters could be found and are listed in Table 3. Zhou et al. [18] suggest different values, Set A, studying the cavitation phenomenon applied to an orifice inserted in a hydraulic circuit and finding good matching between experimental data and simulations results. Zwart et al. [14] propose a set of values, mainly related to water, and authors assert, can also be valid for different fluids and applications, Set B. These sets are also reported in the research of Del Campo et al. [16] applied in several numerical simulations of external gear pumps in cavitating conditions.

**Table 3.** Different values of coefficients used in the simulations.

	$R_{nuc}$	$F_r$	$F_a$
Set A	0.09	0.09	0.01
Set B	0.09	50	0.01

The volume of dissolved air is given by the Bunsen coefficient, which represents the ratio between the volume of gas and the volume of liquid at normal and equilibrium conditions, which is 0.09 for mineral oil. Hence, the density of the nucleation sites was kept fixed and equal to the Bunsen coefficient [16]. The density value of the nucleation sites has been kept constant to highlight the great variability of the results that derive from the uncertainty about the air parameters.

The bubble radius  $R_B$  has been set equal to 0.5  $\mu\text{m}$ , since the gap heights considered are in the same order of magnitude.

In this paper, the vapor cavitation phenomenon has not been considered: This phenomenon begins when the fluid pressure falls below the highest vapor saturated pressure, depending on chemical components of the mineral oil considered, and finishes when the lower vapor saturation pressure is reached. This phenomenon has been neglected, since gaseous cavitation is the first to occur during the working conditions of hydraulic machines.

With the model adopted, when the pressure decreases and reaches the saturation value, i.e., when the dissolved gas is released, the pressure remains constant instead of further decreasing; this limitation will be investigated in future research. In this paper, to overcome this issue and to present a general overview of the behavior of textured surfaces in the presence of gaseous cavitation, the simulations have been carried out setting different saturation pressures. This paper is not focused on improving the modeling of the fluid, however—this research aims to investigate the effect of the gas formation on the bearing capacity of the analyzed design with the fluid model available, also considering the great uncertainty of the cavitation parameters available in the literature.

### 3. Simulation Results

#### 3.1. Single Dimple

To analyze the behavior of a textured surface, the investigation has been initially focused on a single dimple case to understand what dimple geometry permits to obtain better improvements.

A square-shaped dimple has been assumed as reference geometry. In Figure 1, a schematic illustration of the dimple geometry and relative position in respect of the gap is presented, with the geometric features indicated.

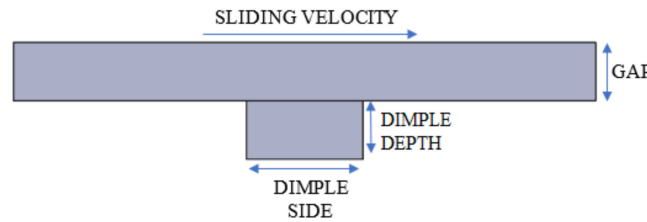


**Figure 1.** Graphic representation of the single dimple configuration with the main geometric features.

The presence of a dimple, on a domain characterized by two flat and parallel surfaces, perturbs the pressure profile because it introduces a divergent area and a following convergent one, as shown in the pressure contour in Figure 2. The presence of a dimple produces a depression area at the beginning of the dimple itself, while an overpressure is generated near the end of the convergent area. The dimensions of the reference domain have been set to permit the pressure gradient, generated by the dimple, to reach the zero value in both the x and y directions: The domain size is 500  $\mu\text{m}$  in the x direction and 300  $\mu\text{m}$  along y.

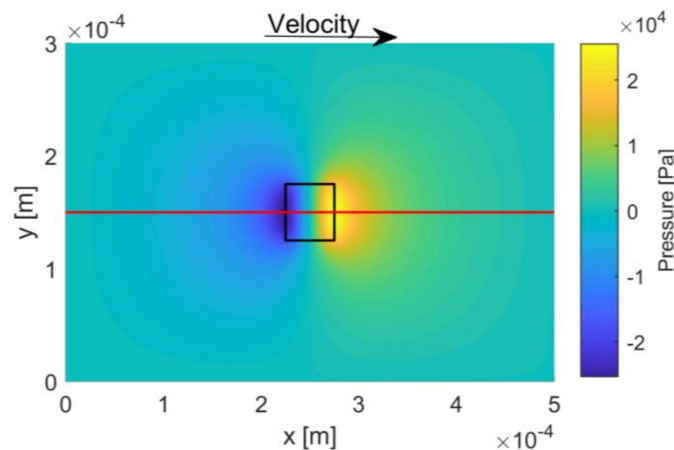


**Figure 2.** Pressure contour of a square dimple with side 50  $\mu\text{m}$  and depth 10  $\mu\text{m}$ . Gap 10  $\mu\text{m}$ , sliding velocity 5 m/s.

The reference velocity adopted for the moving plane is 5 m/s, while the gap is in the order of microns, which are typical values that can be found in many couplings in hydraulic pumps and motors [21,22].

For all the simulations carried out, the boundary conditions are assumed as the open boundary with a relative pressure of 0 bar, and the fluid velocity is normal to the boundary surfaces. The boundary condition for the upper wall is a moving wall with no slip condition, while the lower wall is modeled as a fixed wall and no slip condition [23]. The initial conditions are zero fluid velocity and 0 bar relative pressure inside the domain.

Several simulations have been performed with different combinations of the geometrical features of the dimple and the gap heights. The pressure profiles for different dimple size and gap values are reported in Figure 3. The profiles have been evaluated along the median dimple line on the moving plane, indicated by the red line in Figure 2. The pressure oscillates symmetrically around the mean value, which is the reference pressure set as a boundary condition, and the extent of the oscillation is amplified as the gap decreases.

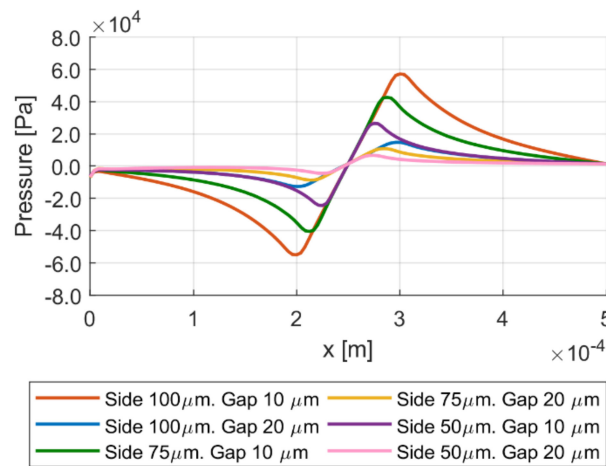


**Figure 3.** The pressure profile perturbation is generated by a square dimple and characterized by different sides and values of the gap. Dimple depth  $10\ \mu\text{m}$ , sliding velocity  $5\ \text{m/s}$ .

The symmetry in the pressure profile is a direct consequence of the symmetry of the dimple geometry: The divergent area is exactly the same as the convergent one, generating a symmetrical pressure profile. These findings could be extended to other dimple shapes that are symmetrical with respect to the direction of motion, such as a rectangular or circular geometry. In Figure 4, the pressure contours of a circular and a rectangular dimple are shown. The surface of both the shapes is the same as the square dimple with side  $50\ \mu\text{m}$ . The pressure profiles are reported in Figure 5: Again, the trend is symmetrical with a null mean value.

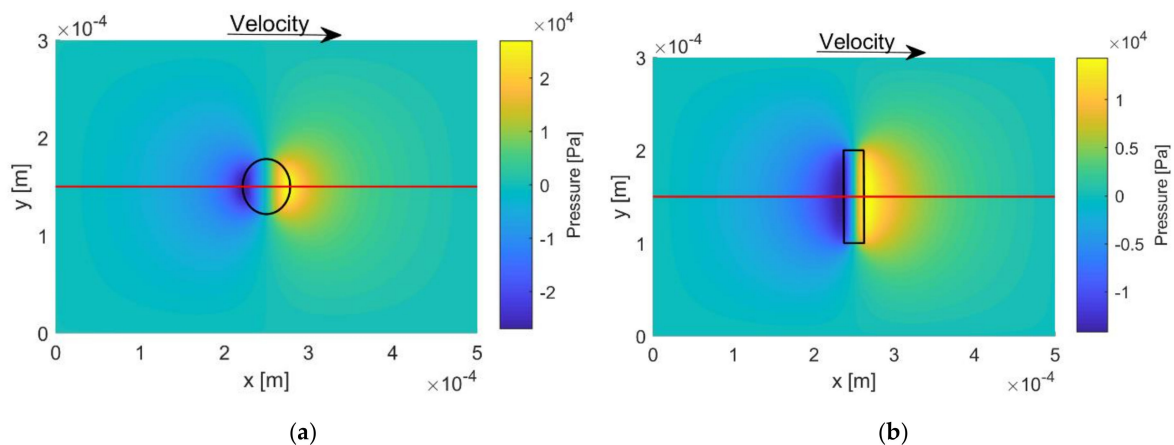


**Figure 4.** (a) Pressure contour of a circular dimple with diameter  $56.4\ \mu\text{m}$  and depth  $10\ \mu\text{m}$ . Gap  $10\ \mu\text{m}$ , sliding velocity  $5\ \text{m/s}$  (b) Pressure contour of a rectangular dimple with side  $100\ \mu\text{m} \times 25\ \mu\text{m}$  and depth  $10\ \mu\text{m}$ . Gap  $10\ \mu\text{m}$ , sliding velocity  $5\ \text{m/s}$ .

The bearing capacity is defined as the integral of the pressure on the moving plane. In the cases presented in previous figures, the pressure integral is always zero: A geometry characterized by a single dimple does not generate a variation in the bearing capacity with respect to the original coupling between two parallel flat surfaces. This conclusion is still valid regardless of the pressure conditions imposed at the boundary, the viscosity of the fluid (which is related to the working temperature), and the sliding velocity of the moving plane.



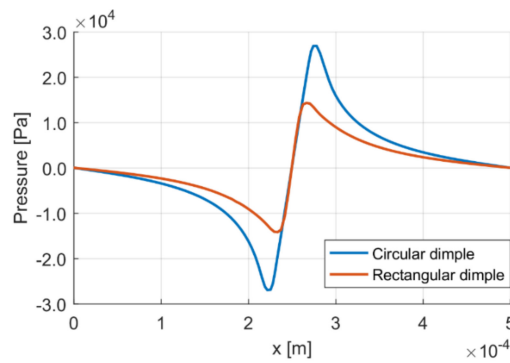


**Figure 5.** Pressure distributions relative to the circle and rectangular case of Figure 4, calculated along the dimples median line.

From the results, shown in Figure 3, the influence of the size of the dimple emerges. Dimples characterized by larger dimensions along the  $x$  direction (i.e., the moving direction) produce a greater pressure profile amplitude, but still symmetrical. Moreover, decreasing the gap generates analogous outcomes, rising the amplitude of the pressure oscillation.

In hydraulic machines, severe operating conditions may lead to very small gap height in internally lubricated couplings. As a consequence, in the case of a single dimple textured surface, the minimum pressure value would drop to a very low value; under these conditions, local cavitation phenomenon can arise.

Figure 6 shows the pressure profile generated by a square dimple as the gap height decreases, adopting the cavitation parameters of Set A with a saturation pressure of  $-0.7$  bar: If the gap height is 5 microns or lower, the pressure falls below the oil saturation threshold, allowing the cavitation inception. Therefore, the symmetry of the pressure profile is distorted, and a bearing capacity is generated.

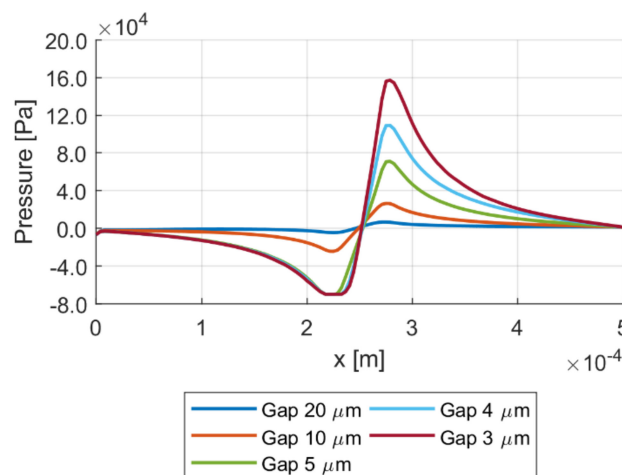


**Figure 6.** Pressure profile of a square dimple with side of  $50\ \mu\text{m}$  and depth  $10\ \mu\text{m}$  for different values of the gap. Sliding velocity  $5\ \text{m/s}$ .

In Figure 7, the bearing capacity produced by a single square dimple of different dimensions is presented, highlighting the benefit achievable in case the gap height is very thin: The trend is more than linear as the gap decreases. The force values are divided by a reference value for confidential reasons.



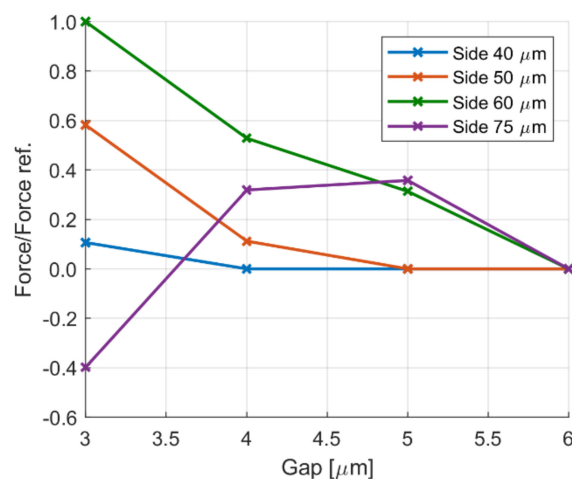


**Figure 7.** Bearing capacity is generated by a square dimple. Influence of the gap for different sizes of the dimple. Dimple depth 10  $\mu\text{m}$ , sliding velocity 5 m/s.

The rising of the bearing capacity, due to the gap reduction may be a useful aspect to balance a possible approach between the coupled surfaces, avoiding the potential condition of direct contact.

In Figure 7 the effect of the size of the dimple is shown, in general a larger dimple improves the bearing capacity of the surface. However, a threshold could be found beyond which the trend is opposite, decreasing the gap the largest dimples present an intensified cavitation phenomenon that generates a wide area at the saturation pressure value. Under these conditions, the fluid at negative pressure affects the pressure rising in correspondence of the convergent zone, limiting the positive maximum pressure value. As a result, the overall pressure integral on the moving plane is negative, worsening the bearing performance of the coupling. As an example, in Figure 8, the air volume fraction is generated by a square dimple with side 75  $\mu\text{m}$  and gap 3  $\mu\text{m}$  is shown. In the figure, only the area where the volume fraction of the air is higher than 1‰ is highlighted. A great amount of air surrounds nearly all the space available in the dimple, and this explains the trend present in Figure 7.

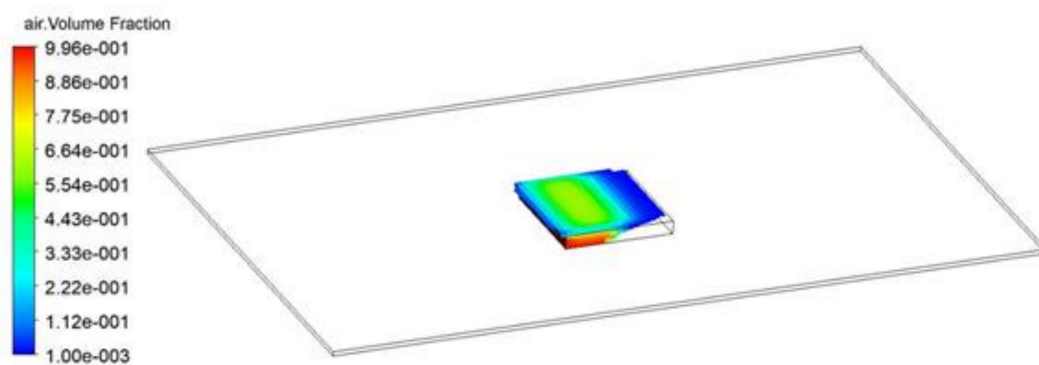


**Figure 8.** The air volume fraction is generated by a square dimple with side of 75  $\mu\text{m}$  and depth 10  $\mu\text{m}$ . Gap 3  $\mu\text{m}$ , sliding velocity 5 m/s. The volumes of the mesh where the volume fraction of air is greater than 1‰ are highlighted.

Another geometric feature considered is the depth of the dimple. This variable has a slight influence on surface performance because it does not change the pressure profile appreciably, as shown in Figure 9.

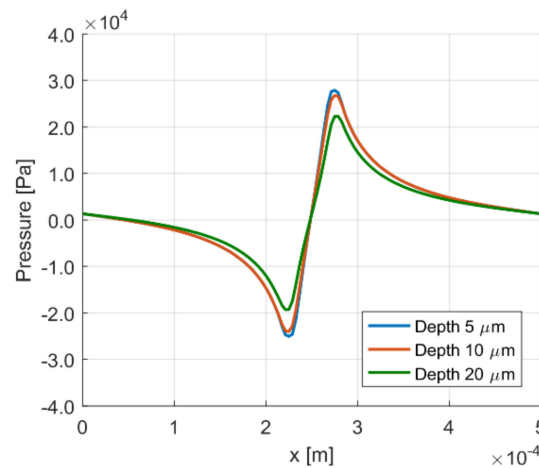


**Figure 9.** Pressure profiles of a square dimple with side 50  $\mu\text{m}$  and gap 10  $\mu\text{m}$ , sliding velocity 5 m/s. Influence of the dimple depth on the pressure distribution.

The performance of a textured surface depends not only on the geometric characteristics of the dimple, but also on the operating conditions, such as the fluid working temperature, i.e., the fluid viscosity, and the sliding velocity of the moving plane.

$$\frac{\partial}{\partial x} \left( h^3 \frac{\partial p}{\partial x} \right) = 6U\eta \frac{dh}{dx} \quad (6)$$

Equation (6) is the simplified Reynolds equation reduced to a one-dimensional form to simply analyze the dependence of the pressure from other variables. The effect on the pressure, due to both the velocity and the fluid viscosity is linear; therefore, the pressure profile in correspondence of the dimple has a greater amplitude with a higher viscosity and higher sliding velocity. Modifying the velocity or the fluid viscosity has an important influence on the cavitation onset: The saturation pressure is reached for greater gap values allowing the generation of greater bearing capacity, but also a greater amount of air is formed, which can negatively affect the coupling.

### 3.2. Full Texturing Surface

In this section, the behavior of a reference domain characterized by a sequence of equally spaced dimples over the entire available surface is presented, Figure 10, realizing a full textured surface.

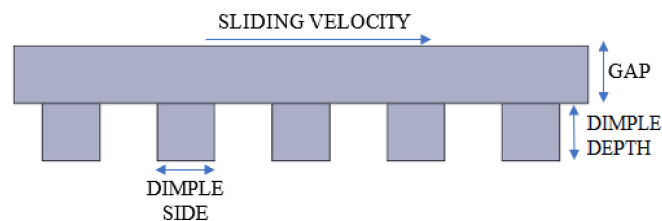


**Figure 10.** Graphic representation of the full texturing configuration with the main geometric features reported.

In this configuration, with the same reference conditions of the previous section, the pressure profile perturbation induced by each dimple is analogous to what happens in the presence of a single dimple. The pressure field exhibits a periodic oscillating trend around the boundary value of pressure, as shown in the pressure contour in Figure 11. Hence, in the case of a full textured domain, it is not possible to achieve any improvement in terms of bearing capacity, and this result is also valid regardless of the geometrical dimensions and shape of the dimples.

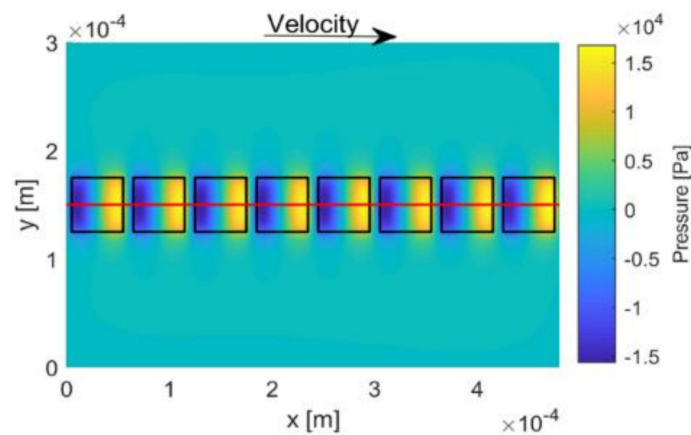


**Figure 11.** Pressure contour of the full texturing configuration. Square dimples with side  $50\ \mu\text{m}$  and depth  $10\ \mu\text{m}$ . Gap  $10\ \mu\text{m}$ , sliding velocity  $5\ \text{m/s}$ .

A gap reduction leads to an increment of the amplitude of the pressure distribution, as for a single dimple case, maintaining the oscillatory trend. In the fully textured configuration, the onset of the cavitation could take place as a result of the reduction of the gap height or by increasing the sliding speed of the moving surface. Figure 12 shows the pressure contour of a domain with gap  $5\ \mu\text{m}$ , assuming the cavitation coefficients of Set A, Table 3, and a saturation pressure of  $-0.7\ \text{bar}$ .

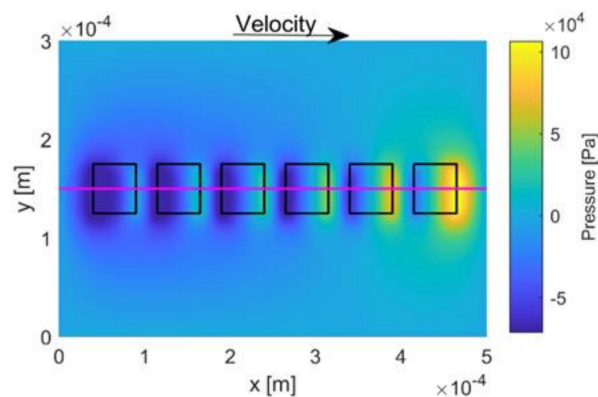


**Figure 12.** Pressure contour of the full texturing configuration. Square dimples with side  $50\ \mu\text{m}$  and depth  $10\ \mu\text{m}$ . Gap  $5\ \mu\text{m}$ , sliding velocity  $5\ \text{m/s}$ .

In this working condition, as can be seen from the pressure contour Figure 12, the first dimples show a considerable cavitating area, that progressively decreases until it completely ceases. After the first dimples, the fluid pressure tends to increase dimple after dimple, since each one gives a positive contribution; however, the overall integral leads to a negative bearing force.

As a further step in analyzing the full textured domain, a multi-row configuration has been studied. In a multi-row configuration, where all dimples are equal to each other and uniformly distributed, the pressure profiles are almost the same as the single row configuration. Figure 12 shows the pressure contour on the moving plane relative to a single row condition, while in Figure 13, there is a generic two-row configuration. The pressure profiles along the dimples median lines are reported in Figure 14; as reported, the pressure profiles are almost the same.

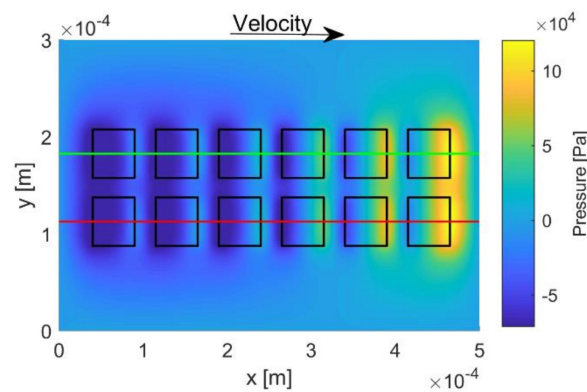


**Figure 13.** Pressure contour of a multi-row configuration. Square dimples with side  $50\ \mu\text{m}$  and depth  $10\ \mu\text{m}$ . Gap  $5\ \mu\text{m}$ , sliding velocity  $5\ \text{m/s}$ .

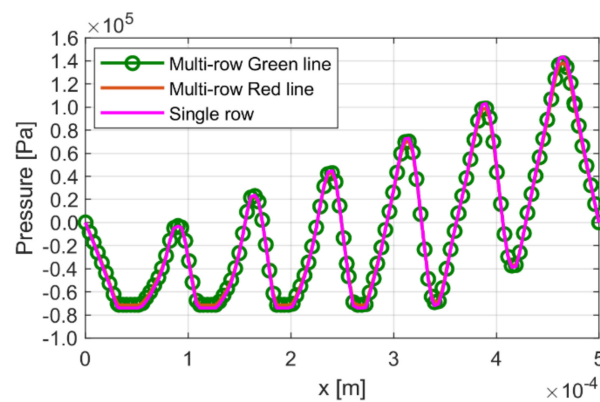


**Figure 14.** Pressure profiles of a full texturing surface with dimples side  $50\ \mu\text{m}$  and gap  $5\ \mu\text{m}$ , sliding velocity  $5\ \text{m/s}$ . Comparison between a single-row configuration and a multi-row.

With the coefficients of Set A of Table 3 in the cavitating area of the domain, a small amount of air is released, which has enough time to be completely reabsorbed, making the cavitation process limited to the first dimples, Figure 15.

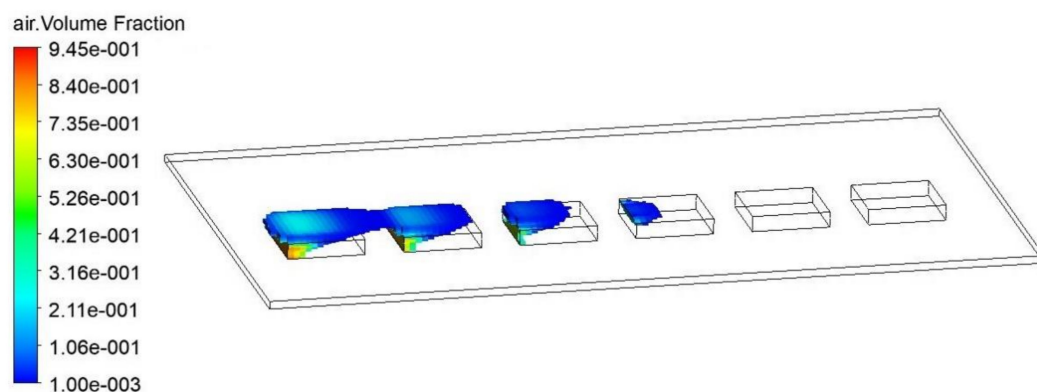


**Figure 15.** The air volume fraction is generated by a full texturing configuration with dimples side  $50\ \mu\text{m}$  and gap  $5\ \mu\text{m}$ , sliding velocity  $5\ \text{m/s}$ . Set A of the cavitation coefficients. Only the portions of the mesh where the volume fraction of air is greater than  $1\text{‰}$  are highlighted.

Using the set B cavitation coefficients, Table 3, different results could be found. The air volume fraction obtained is shown in Figure 16. Compared to Set A, the release coefficient is much higher, while the absorption parameter is the same: As a consequence, the result is that the fluid approaches the

following dimple with a fraction of air preexistent, which limits the pressure rising in correspondence of the convergent zone of the dimple. There is a propagation of the cavitation process very accentuated with the release of a lot of air on the entire domain.

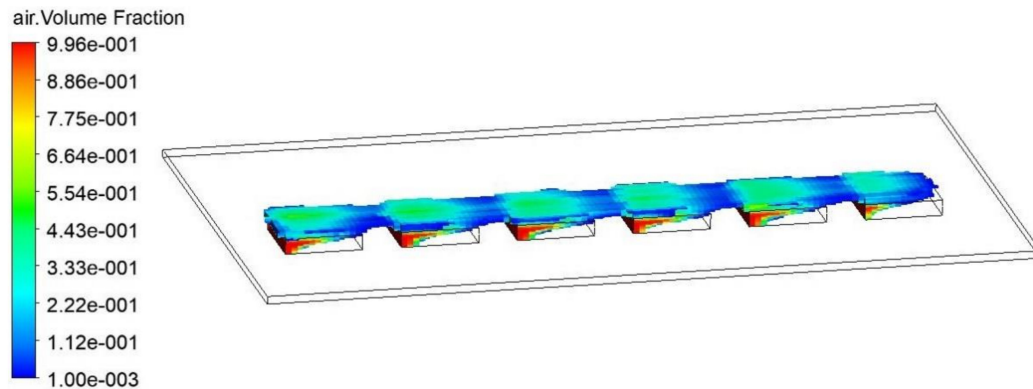


**Figure 16.** The air volume fraction is generated by a full texturing configuration with dimples side  $50\ \mu\text{m}$  and gap  $5\ \mu\text{m}$ , sliding velocity  $5\ \text{m/s}$ . Set B of the cavitation coefficient. Only the portions of the mesh where the volume fraction of air is greater than  $1\text{‰}$  are highlighted.

In all these cases analyzed in this section, the overall hydrodynamic force, generated by the texturing, is still negative.

Regarding the other parameters, such as the depth of the dimple or the fluid viscosity and the sliding velocity, the influence is the same highlighted in the single dimple section.

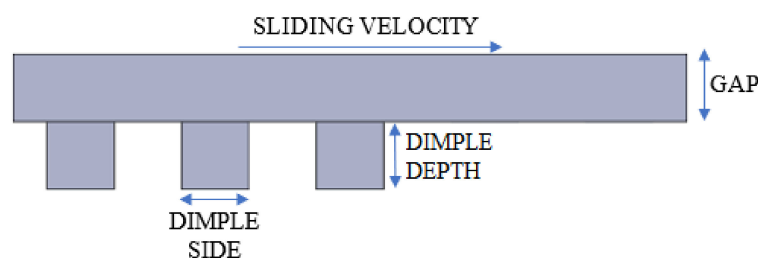
Texturing the whole domain is not useful to increase the bearing capacity of a lubricated coupling in relative motion, since the pressure profile oscillates around a zero value. Moreover, under cavitation conditions, the resulting force is negative.

An important benefit of a fully textured surface is the reduction of the viscous friction coefficient. The average fluid film thickness is increased, due to the introduction of the dimples on a surface, and this permits to reduce the wall shear stress at the moving plane according to the lubrication theory.

### 3.3. Partial Texturing Surface

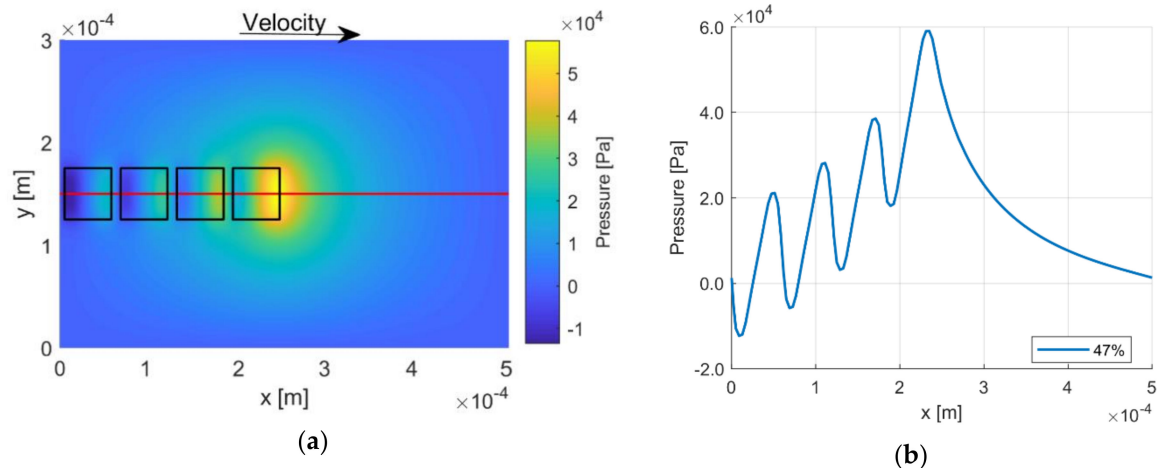
From the analysis of the results obtained on both configurations (single dimple and full texturing) emerges that there are no conditions for which a positive bearing capacity arises, able to oppose the approach between the two coupled surfaces, except in the case of a single dimple in the presence of cavitation. Therefore, to improve the load capacity of a lubricated coupling in any working configuration and condition, more studies are necessary.

Relevant improvements can be achieved by creating a so-called partial texturing, where the dimples are placed only in a part of the available domain, as shown in Figure 17.



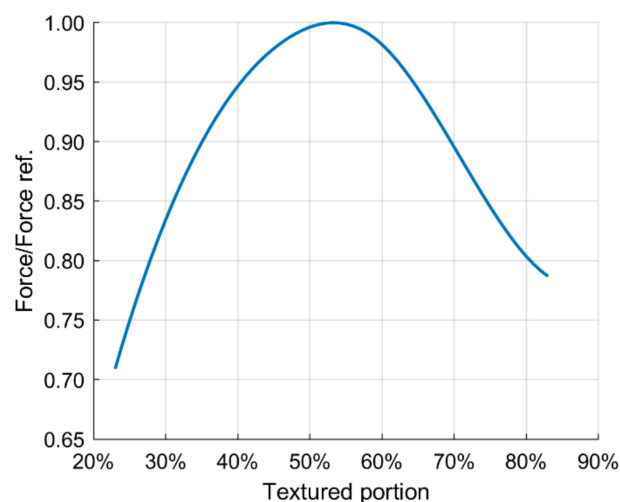
**Figure 17.** Graphic representation of the partial texturing configuration with the main geometric features indicated.

Figure 18a shows the pressure profile relative to the case of texturing almost half of the domain length. In this configuration, differently from the previous cases, the pressure does not oscillate symmetrically around a null mean value; each dimple provides a contribution that locally raises the pressure. In particular, in the proximity of the last dimple, there is a great overpressure that gradually fades, as can be noticed analyzing the pressure profile. The result is the development of a pressure ramp, able to generate a significant bearing capacity.



**Figure 18.** (a) Pressure contour of a partial texturing configuration realized by square dimples with side  $50\ \mu\text{m}$  and depth  $10\ \mu\text{m}$ . Gap  $10\ \mu\text{m}$ , sliding velocity  $5\ \text{m/s}$ . (b) Pressure profiles calculated along the dimples median line, textured portion of 47%. Square dimples with side  $50\ \mu\text{m}$  and gap  $10\ \mu\text{m}$ , sliding velocity  $5\ \text{m/s}$ .

Figure 19 shows a dimensional bearing generated force as a function of the textured portion of the domain. The force is divided by a reference value for confidential reasons. The best condition occurs when the textured portion is 45–60% of the entire domain.



**Figure 19.** Force is generated by the partial texturing surface as a function of the textured portion. Square dimples with side  $50\ \mu\text{m}$  and gap  $10\ \mu\text{m}$ , sliding velocity  $5\ \text{m/s}$ .

In partial texturing, surface cavitation could occur under the same operating conditions as in other configurations, like decreasing the gap or increasing the sliding velocity. In this section, the sliding velocity is set to  $10\ \text{m/s}$  to make the phenomenon of cavitation more noticeable to better evaluate its effects on the pressure distribution.

The bearing force is generated by the surface in the partial texturing configuration shows different trends, both with the variation of the set of fluid parameters and with the air release saturation pressure.

Figure 20 shows the force as a function of the gap; these simulations were carried out with Set A cavitation parameters. The results are strongly influenced by the saturation pressure, i.e., the pressure at which the gas starts to be released.

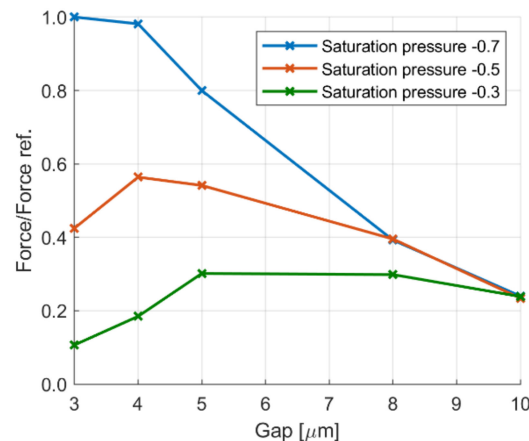


**Figure 20.** Bearing capacity is generated by a partial texturing configuration. Influence of the gap for different values of saturation pressure. Set A cavitation coefficients. Square dimple with side 50  $\mu\text{m}$  and depth 10  $\mu\text{m}$ , sliding velocity 10 m/s.

The trends for high gap heights are due to the different amount of air that is released: As can be seen in Figure 21, if a higher saturation pressure is considered, a larger amount of air is released: As a general trend, it occupies most of the volume of the dimples, and this negatively influences the force generated by the surface. In Figure 21, the portion where the volume fraction of the air is higher than 10% is highlighted. For high gap values (e.g., 8  $\mu\text{m}$ ) the best performance can be achieved if saturation pressure is set to a low value (−0.7 bar), since a less amount of gas is released, allowing a greater bearing capacity.

In Figure 22, the pressure profiles related to the 8  $\mu\text{m}$  gap condition are shown. Confirming the previous air volume fraction behavior, the fluid remains at the saturation point for a longer time as a higher saturation pressure value is considered: This leads to the release of a greater quantity of air. On the contrary, at a lower saturation pressure, less air is released, and oil pressurization begins at an earlier stage of the textured domain, and therefore, allows obtaining a higher pressure.

As soon as the gap height becomes small, a greater amount of air is released, regardless of the saturation pressure considered. As shown in Figure 23, for a gap height of 3 microns, cavitation affects almost all the dimples present in the domain.

For low gap values, the behavior of a partially textured surface depends on the quantity of air released. The saturation pressure value affects the time during which the fluid remains at the saturation pressure releasing air. With a low saturation pressure (−0.7 bar), the textured surface allows obtaining a large overpressure value that reduces the effect of cavitation, especially on the last dimple. On the other hand, with a higher saturation pressure (−0.3 bar), the amount of air present in the last dimple is large, affecting the maximum pressure reachable with the consequence of reducing the generated force, Figure 24.



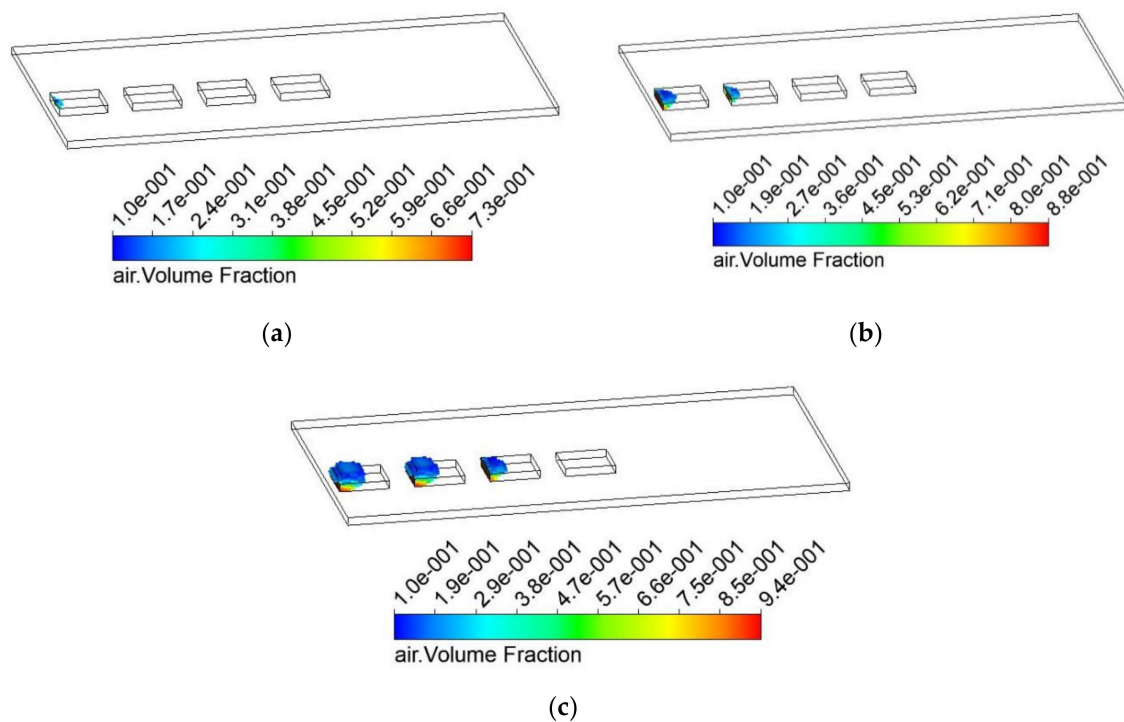


**Figure 21.** The air volume fraction is generated by a partial texturing configuration with dimples side  $50\ \mu\text{m}$  and gap  $8\ \mu\text{m}$ , sliding velocity  $10\ \text{m/s}$ . Set A of the cavitation coefficients. Only the portions of the mesh where the volume fraction of air is greater than 10% are highlighted. (a) Saturation pressure  $-0.7\ \text{bar}$ ; (b) Saturation pressure  $-0.5\ \text{bar}$ ; (c) Saturation pressure  $-0.3\ \text{bar}$ .

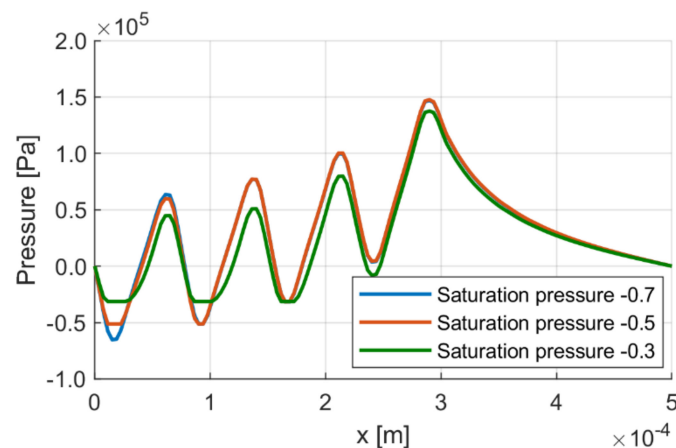


**Figure 22.** Pressure profiles calculated along the dimples median line, considering different saturation pressure values. Square dimples with side  $50\ \mu\text{m}$  and gap  $8\ \mu\text{m}$ , sliding velocity  $10\ \text{m/s}$ . Set A of the cavitation coefficients.

To investigate the effects of assuming different cavitation coefficients available in the literature, simulations were carried out using the set B coefficients of Table 3. Figure 25 shows the force as a function of the gap and the saturation pressure for set B coefficients. It can be noted that these trends, compared to those of set A coefficients, shown in Figure 20, are very different. In set B, the air absorption coefficient is the same as set A, while the air release parameter is much higher: This greatly influences the behavior of the textured surface.

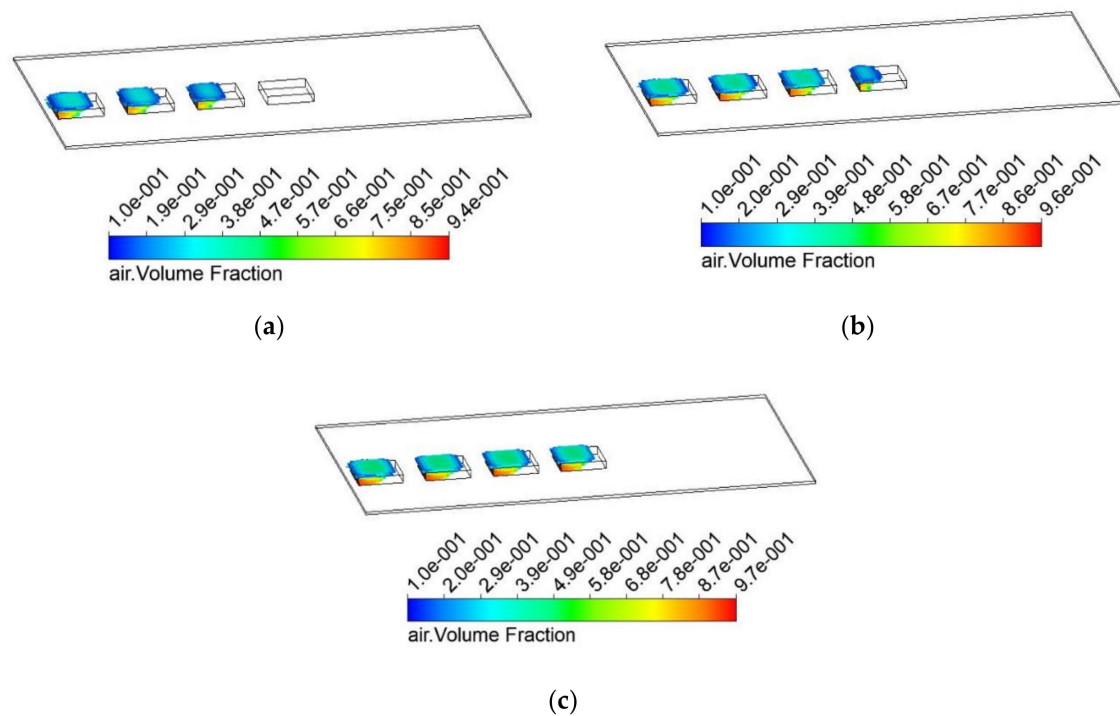


**Figure 23.** The air volume fraction is generated by a partial texturing configuration with dimples side  $50\ \mu\text{m}$  and gap  $3\ \mu\text{m}$ , sliding velocity  $10\ \text{m/s}$ . Set A of the cavitation coefficients. Only the portions of the mesh where the volume fraction of air is greater than 10% are highlighted. (a) Saturation pressure  $-0.7\ \text{bar}$ ; (b) Saturation pressure  $-0.5\ \text{bar}$ ; (c) Saturation pressure  $-0.3\ \text{bar}$ .

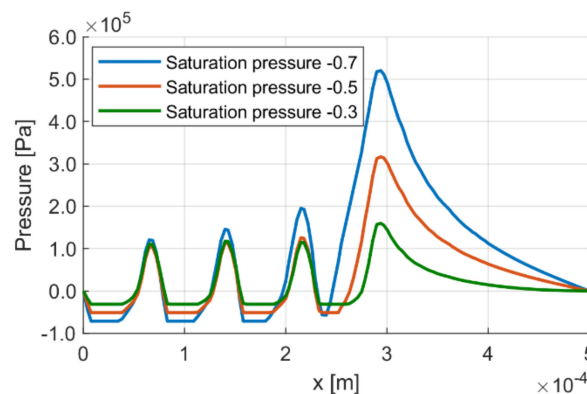


**Figure 24.** Pressure profiles calculated along the dimples median line at different saturation pressures. Square dimples with side  $50\ \mu\text{m}$  and gap  $3\ \mu\text{m}$ , sliding velocity  $10\ \text{m/s}$ . Set A of the cavitation coefficients.

The trend for high gap values is due to the different amount of air that is released; however, unlike the previous case, the generated force is positive only for the lowest saturation pressure value. Figure 26 shows the air volume fraction with a gap of  $8\ \mu\text{m}$ : With a low saturation pressure ( $-0.7\ \text{bar}$ ), a small amount of air is released, very similar to the case of Set A and for this reason, both the pressure curve, Figure 27, and the generated force are the same as the previous case. However, with a higher saturation pressure ( $-0.3\ \text{bar}$ ), the cavitation phenomenon is very intense, and in some cases, the air does not have enough time to be completely reabsorbed in the little path between one dimple and the following one. Propagation of the cavitation phenomenon occurs that compromises the performance

of the textured surface. For this reason, the generated force with a high saturation pressure ( $-0.3 \div -0.5$  bar) is negative.

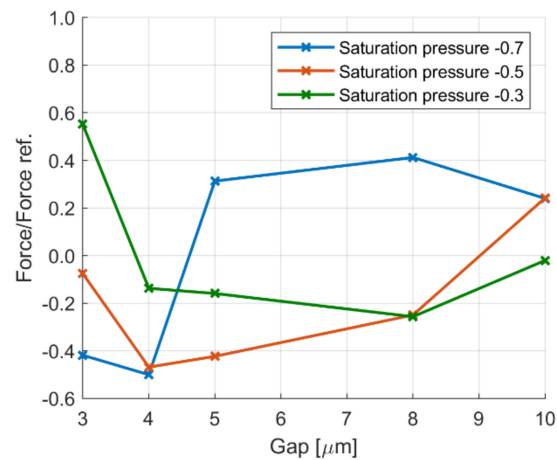


**Figure 25.** Bearing capacity is generated by a partial texturing configuration. Influence of the gap for different values of saturation pressure. Set B cavitation coefficients. Square dimple with side  $50 \mu\text{m}$  and depth  $10 \mu\text{m}$ , sliding velocity  $10 \text{ m/s}$ .

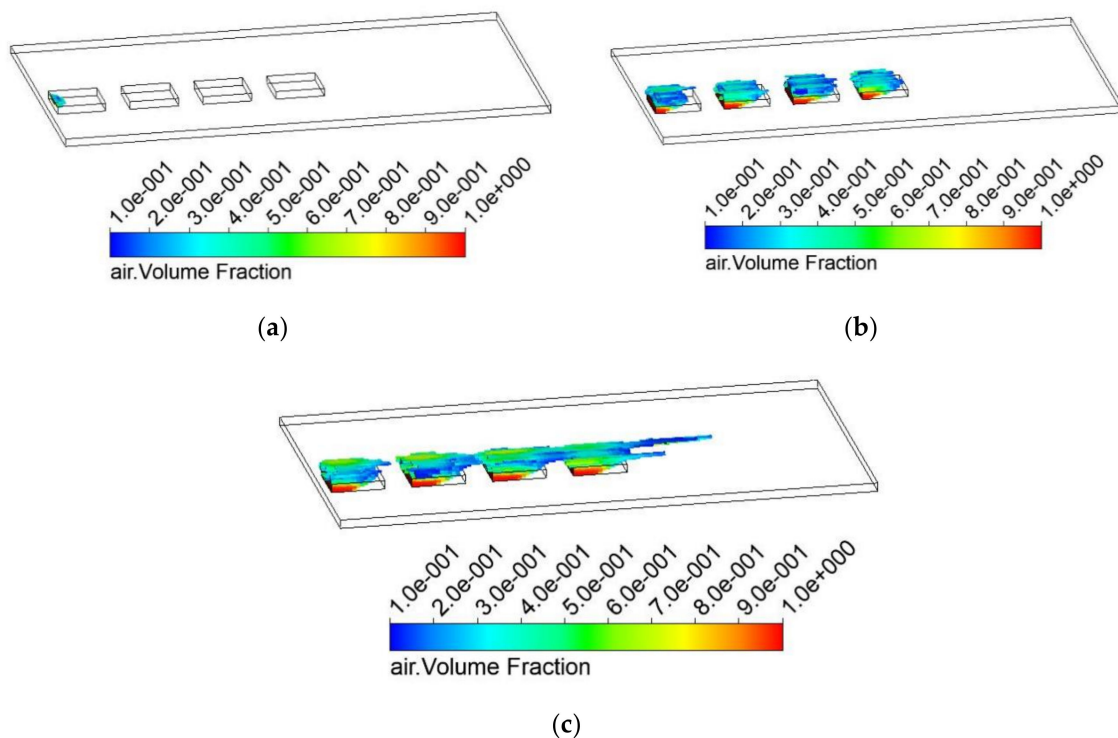


**Figure 26.** The air volume fraction is generated by a partial texturing configuration with dimples side  $50 \mu\text{m}$  and gap  $8 \mu\text{m}$ , sliding velocity  $10 \text{ m/s}$ . Set B of the cavitation coefficients. Only the portions of the mesh where the volume fraction of air is greater than 10% are highlighted. (a) Saturation pressure  $-0.7$  bar; (b) Saturation pressure  $-0.5$  bar; (c) Saturation pressure  $-0.3$  bar.

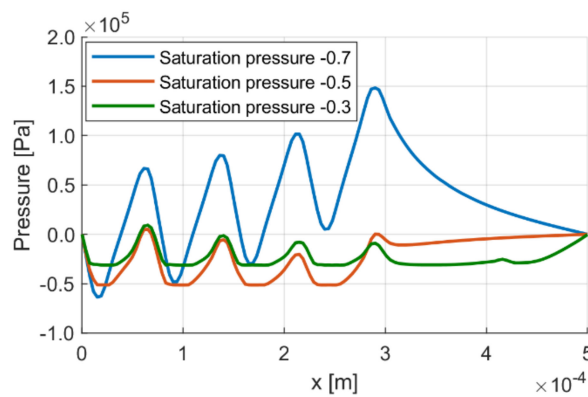


**Figure 27.** Pressure profiles calculated along the dimples median line at different saturation pressures. Square dimples with side  $50\ \mu\text{m}$  and gap  $8\ \mu\text{m}$ , sliding velocity  $10\ \text{m/s}$ . Set B of the cavitation coefficients.

Figure 27 shows the pressure profile for a gap of  $8\ \mu\text{m}$ . Cavitation occurs very intensely, and for high saturation pressure values ( $-0.3\ \text{bar}$ ), the pressure profile always remains below atmospheric pressure, and partial texturing is not able to guarantee an overpressure capable of counteracting the negative effect of cavitation. With a low saturation pressure ( $-0.7\ \text{bar}$ ), a slight cavitation phenomenon occurs and remains confined to a small portion of the first dimple. In this situation, the curve has a growing trend, and an overpressure could be generated, allowing a positive integration of the pressure on the moving plane.

By further decreasing the gap, the trend changes: The force increases for each configuration and is greater as the saturation pressure increases. Under these conditions, the amount of air released is not very different among the various cases, as can be seen in Figure 28: Therefore, the textured surface generates a greater bearing capacity where the gas, as well as the fluid, presents a higher minimum pressure ( $-0.3\ \text{bar}$ ).

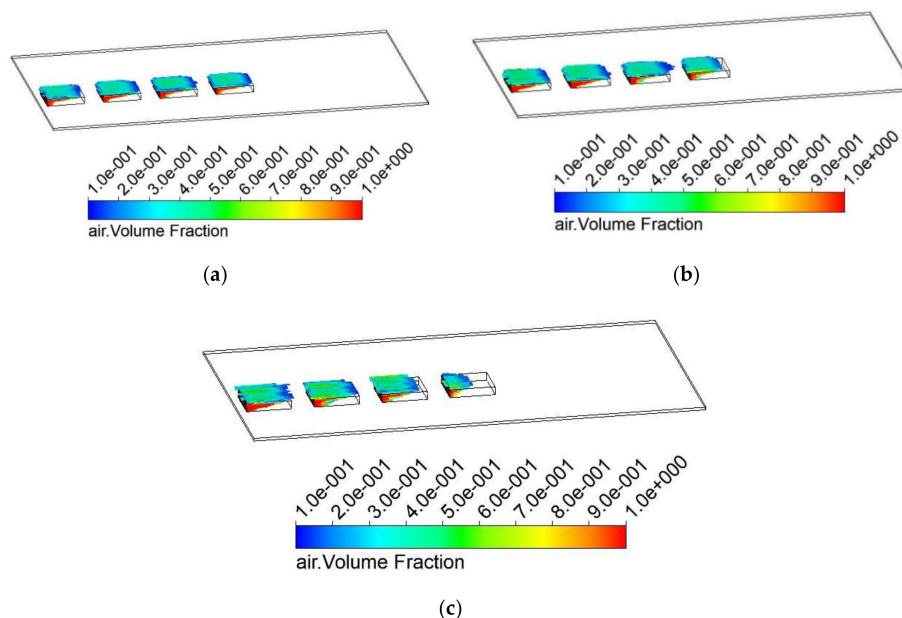


**Figure 28.** The air volume fraction is generated by a partial texturing configuration with dimples side  $50\ \mu\text{m}$  and gap  $3\ \mu\text{m}$ , sliding velocity  $10\ \text{m/s}$ . Set B of the cavitation coefficient. Only the portions of the mesh where the volume fraction of air is greater than 10% are highlighted. (a) Saturation pressure  $-0.7\ \text{bar}$ ; (b) Saturation pressure  $-0.5\ \text{bar}$ ; (c) Saturation pressure  $-0.3\ \text{bar}$ .

To better understand what happens for low gap values, in Figure 29, the pressure profiles concerning the gap of 3  $\mu\text{m}$  are shown. At low gap heights with this set of parameters, the release condition of air is reached almost instantaneously regardless of the saturation pressure, while reabsorption is always slow. The increment of pressure generated at each dimple is greater if the saturation pressure is the highest ( $-0.3$  bar). The overall effect is a progressive greater over-pressure in the gap, due to the sequence of dimples, which reduces the cavitation effect, especially on the last dimple where a higher overpressure is reached, contributing to obtain a positive bearing force.

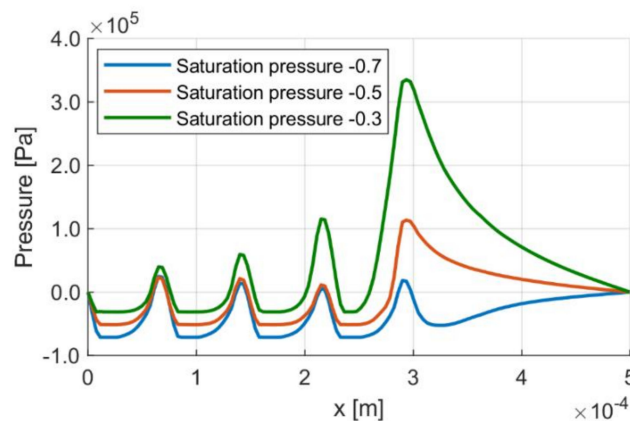


**Figure 29.** Pressure profiles calculated along the dimples median line at different saturation pressures. Square dimples with side 50  $\mu\text{m}$  and gap 3  $\mu\text{m}$ , sliding velocity 10 m/s. Set B of the cavitation coefficient.

The partial textured configuration still allows reducing the viscous friction coefficient, but to a lesser extent than the full textured case. The average fluid film thickness is increased only on a portion of the entire domain, and consequently, the reduction of the wall shear stress is lower.

#### 4. Discussion

The simulations carried out show that the cavitation phenomenon strongly affects the bearing capacity of a textured surface. It is hard to find in literature a sole set of parameters able to describe comprehensively the dynamics of air release and reabsorption. When cavitation occurs, the characteristic time of the transient in which the phase of the fluid change is very rapid, and it is comparable to the time taken by the fluid to move from one dimple to the next.

Further investigations have been carried out to verify if a greater distance between the dimples can give the air more time to be reabsorbed, and therefore, reduce the overall amount of air in the domain. In Figure 30, the dimension of the dimples along the moving direction has been decreased, leaving the textured portion unaltered—this allows obtaining a greater spacing between the dimples. Consequently, the air has a larger space available before approaching the next dimple, and therefore, has more time to be completely reabsorbed. In this condition, the overall generated force by the coupling is nearly the same as the starting condition, but with the advantage of having less air in the gap.

The onset of cavitation and its propagation through the dimples add another important variable to be investigated during the design phase of textured surfaces, since the geometric features of the surface influence the tribological behavior of the coupling, especially when the gap is very small. Moreover, to characterize in detail the cavitation process, an accurate model of the fluid is essential, because even slight variations in the air release and air absorption coefficients considerably modify the pressure distribution. This paper takes advantage of literature best references on this topic, but, as shown in Table 3, the coefficients present a relevant uncertainty, at which must be added to the lack of knowledge of the exact composition of the fluid. However, the research presented in this paper can contribute to point out how the characteristic time of the cavitation phenomenon becomes

relevant when the fluid process involves transient phenomena, due to the geometric variation that, being very small, occurs in a very short time. Furthermore, the great variability of the results presented in this paper is due to the uncertainty of the release and absorption coefficients of the air; the results presented contribute to defining the possible scenarios that could happen between the textured surfaces analyzed. The differences between the result presented in Figures 20 and 25 well remark these issues; for example, focusing on the case at saturation pressure equal to  $-0.5$  bar, the results at lower gap values are always negative when the set B parameters are considered, while are always positive when the set A is considered. Therefore, a reliable fluid model could resolve this uncertainty.

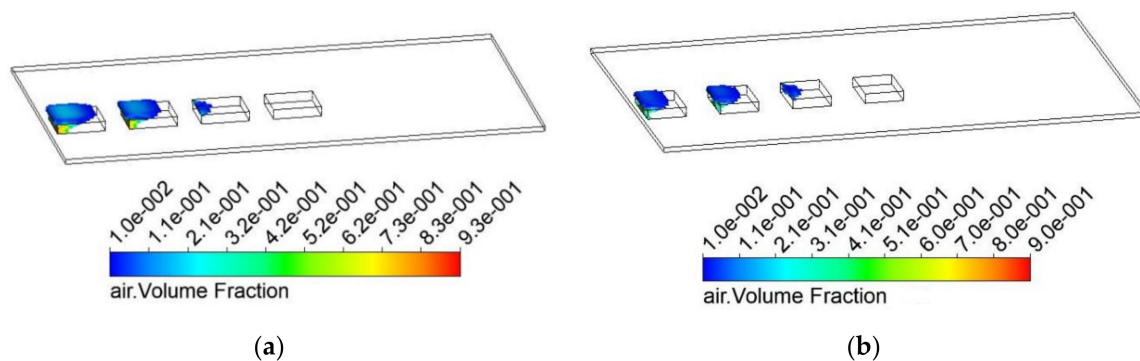


**Figure 30.** The air volume fraction is generated by a partial texturing configuration using Set A cavitation coefficients and a saturation pressure of  $-0.7$  bar. Gap  $5\text{ }\mu\text{m}$ , sliding velocity  $10\text{ m/s}$ . Highlighted only the volumes of the mesh where the volume fraction of air is greater than 1%. (a) Dimples side  $50\text{ }\mu\text{m}$ . (b) Dimples side  $40\text{ }\mu\text{m}$ . The textured portion remains unchanged.

## 5. Conclusions

In this paper, the preliminary results of research concerning textured surfaces for improving the performance of lubricated couplings in hydraulic machines have been presented. The research has highlighted that some benefits in the tribological properties of a lubricated coupling between sliding surfaces could be achieved by introducing a textured surface.

The design stage, in which the dimples geometry and their spatial distribution has to be defined, is a challenge, due to the high number of variables involved.

Texturing only the first portion of the available domain appears to be the best solution from the CFD simulations performed. The simulations have been carried out—including the cavitation phenomenon, which could significantly influence the bearing performance of the coupling. It has also been investigated how the air bubbles are released and then reabsorbed into the fluid, correlating the characteristic times of the process with the pressure evolution through the dimples. The cavitation parameters of the fluid model are very important to simulate the cavitation propagation and its effect on the pressure distribution, in a fluid domain where the geometric variations are very small and affect the fluid process in a very short time. There is great uncertainty about the release and absorption coefficients of air, and this paper presents an investigation of these effects based on the fluid model data available in the literature, presenting the possible scenarios that could happen.

Future developments should include a further study of dimples geometry and distribution: The effects, due to different dimple shape and orientation will be analyzed.

Furthermore, experimental tests of different textured configurations will be performed to check the performance improvements of hydraulic machines.



**Author Contributions:** Conceptualization, P.C. and F.S.; methodology, P.C. and F.S.; simulations, F.S.; formal analysis, F.S.; investigation, P.C., F.S., M.R. (Massimo Rundo), A.L., M.R. (Manuel Rigosi); writing—original draft preparation, F.S.; writing—review and editing, P.C., F.S., M.R. (Massimo Rundo), A.L., M.R. (Manuel Rigosi); supervision, P.C.; All authors have read and agreed to the published version of the manuscript.

**Funding:** This research received no external funding.

**Acknowledgments:** The authors would like to acknowledge the active support of this research by Casappa S.p.A., Parma, Italy.

**Conflicts of Interest:** The authors declare no conflict of interest.

## Nomenclature

$R_B$	Bubble radius [m]
$\sigma$	Surface tension [Pa]
$p$	Pressure [Pa]
$\rho_f$	Liquid density [kg/m <sup>3</sup> ]
$N_B$	Bubbles per unit volume
$rg$	Volume fraction
$\dot{m}_{fg}$	Interphase mass transfer rate [kg/s]
$h$	Gap [m]
$U$	Sliding velocity [m/s]
$\eta$	Dynamic fluid viscosity [Pa s]

## References

1. Ibatan, T.; Uddin, M.S.; Chowdhury, M.A.K. Recent development on surface texturing in enhancing tribological performance of bearing sliders. *Surf. Coat. Technol.* **2015**, *272*, 102–120. [\[CrossRef\]](#)
2. Yu, H.; Wang, X.; Zhou, F. Geometric Shape Effects of Surface Texture on the Generation of Hydrodynamic Pressure Between Conformal Contacting Surfaces. *Tribol. Lett.* **2010**, *37*, 123–130. [\[CrossRef\]](#)
3. Dobrica, M.B.; Fillon, M.; Pascovici, M.D.; Cicone, T. Optimizing surface texture for hydrodynamic lubricated contacts using a mass-conserving numerical approach. *Proc. Inst. Mech. Eng. Part J J. Eng. Tribol.* **2010**, *224*, 737–750. [\[CrossRef\]](#)
4. Rahmani, R.; Shirvani, A.; Shirvani, H. Optimization of Partially Textured Parallel Thrust Bearings with Square-Shaped Micro-Dimples. *Tribol. Trans.* **2007**, *50*, 401–406. [\[CrossRef\]](#)
5. Etsion, I.; Halperin, G.; Brizmer, V.; Klingerman, Y. Experimental investigation of laser surface textured parallel thrust bearings. *Tribol. Lett.* **2003**, *17*, 295–300. [\[CrossRef\]](#)
6. Klingerman, Y.; Etsion, I. Analysis of the Hydrodynamic Effects in a Surface Textured Circumferential Gas Seal. *Tribol. Trans.* **2001**, *44*, 472–478. [\[CrossRef\]](#)
7. Razzaque, M.M.; Faisal, T.R. Performance of Mechanical Face Seals with Surface Micropores. *J. Mech. Eng.* **2008**, *37*, 77–80. [\[CrossRef\]](#)
8. Brizmer, V.; Klingerman, Y.; Etsion, I. A Laser Surface Textured Parallel Thrust Bearing. *Tribol. Trans.* **2003**, *46*, 397–403. [\[CrossRef\]](#)
9. Rundo, M.; Altare, G.; Casoli, P. Simulation of the filling capability in vane pumps. *Energies* **2019**, *12*, 283. [\[CrossRef\]](#)
10. Casoli, P.; Bedotti, A.; Campanini, F.; Pastori, M. A methodology based on cyclostationary analysis for fault detection of hydraulic axial piston pumps. *Energies* **2018**, *11*. [\[CrossRef\]](#)
11. Casoli, P.; Campanini, F.; Bedotti, A.; Pastori, M.; Lettini, A. Overall Efficiency Evaluation of a Hydraulic Pump with External Drainage Through Temperature Measurements. *J. Dyn. Syst. Meas. Control Trans. ASME* **2018**, *140*. [\[CrossRef\]](#)
12. Casoli, P.; Pastori, M.; Scolari, F. A multi-fault diagnostic method based on acceleration signal for a hydraulic axial piston pump. *AIP Conf. Proc.* **2019**, 2191. [\[CrossRef\]](#)
13. Rundo, M.; Squarcini, R.; Furno, F. Modelling of a Variable Displacement Lubricating Pump with Air Dissolution Dynamics. *SAE Int. J. Engines* **2018**, *11*. [\[CrossRef\]](#)
14. Zwart, P.; Belamri, T. A Two-Phase Flow Model for Predicting Cavitation Dynamics. In Proceedings of the 5th International Conference on Multiphase Flow, Yokohama, Japan, 30 May–4 June 2004.



15. Escaler, X.; Roig, R.; Hidalgo, V. Sensitivity Analysis of Zwart-Gerber-Belamri Model Parameters on the Numerical Simulation of Francis Runner Cavitation. In Proceedings of the 10th International Symposium on Cavitation—CAV2018, Baltimore, MD, USA, 14–16 May 2018. [[CrossRef](#)]
16. Del Campo, D.; Castilla, R.; Raush, G.A.; Montero, P.J.G.; Cordina, E. Numerical Analysis of External Gear Pumps Including Cavitation. *J. Fluids Eng.* **2012**, *134*. [[CrossRef](#)]
17. Zhou, J.; Hu, J.; Yuan, S. Modelling bubble evolution in air-oil mixture with a simplified method. *Proc. Inst. Mech. Eng. Part C J. Mech. Eng. Sci.* **2016**, *230*, 2865–2871. [[CrossRef](#)]
18. Zhou, J.; Hu, J.; Jing, C. Lumped parameter modelling of cavitating orifice flow in hydraulic systems. *J. Mech. Eng.* **2016**, *62*, 373–380. [[CrossRef](#)]
19. Zhou, J.; Vacca, A.; Manhartgruber, B. A Novel Approach for the Prediction of Dynamic Features of Air Release and Absorption in Hydraulic Oils. *J. Fluids Eng.* **2013**, *135*, 091305. [[CrossRef](#)]
20. Vacca, A.; Klop, R.; Ivantysynova, M. A numerical approach for the evaluation of the effects of air release and vapour cavitation on effective flow rate of axial piston machines. *Int. J. Fluid Power* **2010**, *11*, 33–45. [[CrossRef](#)]
21. Koc, E.; Hooke, C.J. An experimental investigation into the design and performance of hydrostatically loaded floating wear plates in gear pumps. *Wear* **1997**, *209*, 184–192. [[CrossRef](#)]
22. Ivantysyn, R.; Shorbagy, A.; Weber, J. Analysis of the Run-in Behavior of Axial Piston Pumps. In Proceedings of the 2018 Global Fluid Power Society PhD Symposium (GFPS), Samara, Russia, 18–20 July 2018. [[CrossRef](#)]
23. Stachnik, M.; Jakubowski, M. Multiphase model of flow and separation phases in a whirlpool: Advanced simulation and phenomena visualization approach. *J. Food Eng.* **2020**. [[CrossRef](#)]

**Publisher’s Note:** MDPI stays neutral with regard to jurisdictional claims in published maps and institutional affiliations.



© 2020 by the authors. Licensee MDPI, Basel, Switzerland. This article is an open access article distributed under the terms and conditions of the Creative Commons Attribution (CC BY) license (<http://creativecommons.org/licenses/by/4.0/>).